Biomedical Signal Processing and Control 110 (2025) 108223

Contents lists available at ScienceDirect

Biomedical Signal Processing and Control

journal homepage: www.elsevier.com/locate/bspc

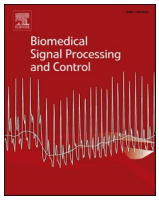

A contactless human vital sign monitoring system using a Doppler radar

Qi Yong, Yifan Zhao *

Faculty of Engineering and Applied Sciences, Cranfield University, Cranfield MK43 0AL, UK

ARTICLE INFO

Keywords:
Contactless
Vital signs
Doppler radar
Parametric filter designing
Digital signal processing

ABSTRACT

Traditional vital signs monitoring methods are associated with certain limitations, such as requiring direct skin contact, causing potential distractions from sensors, and being susceptibility to electromagnetic interferences. Non-contact measurement methods have attracted growing interest but existing solutions face challenges in terms of working distance, accuracy, lack of temporal resolution, and applications in real-time heartbeat detection. This study introduces a novel non-contact vital sign monitoring system based on a K-band radar with dedicated algorithms for demodulation, parametric filter design, and self-adapting real-time heartbeat detection and extraction. This system provides precise and reliable per-beat heartrate detection and measurement, under a wide range of distances and working conditions, achieving superior performances and functionalities compared to existing contact-based implementations. By comparing with photoplethysmography and phonocardiogram sensors, the proposed system achieved real-time accurate per-beat heart rate measurement, with a relative root mean squared error of < 5 % for working distance of up to 3.2 m. Additionally, it can detect apneas and abnormal breathing activities, while also generating phonocardiogram and vibrography signals as a contactless virtual stethoscope. We anticipate that the solution will enable a wide range of applications including critical personnel monitoring, home and healthcare surveillance, self-assisted public health devices, and rescue operations.

1. Introduction

Monitoring vital signs related to cardiovascular and respiration functions not only helps assess a person's general physical state but also assists in the diagnosis of various diseases. It also could provide an assistive role in the development of human–machine interfaces as these signs are already used for evaluations of cognitive load, mental stress, emotion and so on. The monitoring of cardiac activity typically involves methods such as auscultation, photoplethysmography (PPG), phonocardiogram (PCG), and electrocardiography (ECG). With accurate measurements, a heart rhythm trend can be obtained, plotted, and analysed. From this trend, several rhythmic parameters, such as heart rate variation (HRV), can be calculated. Monitoring respiration allows the detection of apneas and abnormal breathing patterns, such as over-respiration or choking incidents. Acoustic information obtained through respiration auscultation can also aid in the diagnosis of pulmonary disease or airway restrictions.

Traditional vital signs measuring and monitoring systems often require direct skin contact to obtain accurate measurements. The presence of lead wires and attached sensors can lead to obstructions, disturbances, and distractions for the individuals being monitored. This introduces risks, particularly in scenarios such as driver monitoring or field rescue operations. Additionally, the constant wearing of sensors can be perceived as invasive, potentially affecting the mood of the person under observation. Traditional methods are also susceptible to artefacts and interferences due to their inherent nature. For instance, PPG and acoustic auscultation pick up subtle acoustic vibrations on the chest wall, making them susceptible to environmental acoustic noise, vibrations, and subject movements. Environmental noise can easily overpower the cardiac acoustic signal, resulting in a low signal-to-noise ratio (SNR). Furthermore, movements and vibrations can generate artefacts when the chest wall rubs against the sensor membrane, creating noise and attenuating the signals. PPG, while less susceptible to environmental acoustic noises due to its light sensor, often produces signals with low amplitudes. This necessitates strong amplification, making it sensitive to ambient light changes and fluctuations in skin pressure. The human body's structure and blood vessels can also induce artefacts due to movements and pressure variations. Therefore, PPG is typically carried out in static environments with proper light shielding.

ECG measures cardiac electrical activities by picking up microscopic electrical potentials and amplifying them. These potentials are generated during cardiac cycles by the depolarisation and polarisation of

* Corresponding author.
E-mail address: yifan.zhao@cranfield.ac.uk (Y. Zhao).

https://doi.org/10.1016/j.bspc.2025.108223
Received 24 November 2024; Received in revised form 15 April 2025; Accepted 14 June 2025
Available online 2 July 2025
1746-8094/© 2025 The Author(s). Published by Elsevier Ltd. This is an open access article under the CC BY license (http://creativecommons.org/licenses/by/4.0/).

cardiac nerves and muscles. These signals have low amplitude and thus require high-gain electrical amplification, making them vulnerable to electromagnetic interferences. Therefore, it is practically impossible to use ECG in environments with such interferences. ECG also requires steady and firm electrode skin contacts to establish an effective conduction loop. Any fluctuations in electrodes can distort measuring planes, vectors, and the signals themselves.

Given the limitations and constraints of traditional methods, there is a strong need for a reliable and portable contactless vital sign measurement technique for certain applications. This paper introduces an innovative high-performance non-contact vital sign monitoring system utilising a K-band radar in conjunction with specialised filters and parameter extraction algorithms. The system can effectively measure a person's cardiovascular and respiration behaviours simultaneously. The integration of a PPG sensor and a PCG sensor serves to validate the performance of monitoring cardiovascular signs based on instrumental and experimental tests.

2. Related works

A relatively popular approach to measure cardiovascular signs is by inspecting skin colour changes or micro displacements using optical sensors. Researchers such as Zhang *et al.* [1], Lewandowska *et al.* [2], Bush [3] and Kayani [4] have demonstrated the implementation of pulse signal monitoring based on videos. This approach uses common webcams to capture videos of the human face and employs colour tracing algorithms to parse the micro changes in RGB colour caused by pulsating blood vessels. It can provide an approximation of the heart rate by applying the Fourier Transform to the parsed signal. However, it is highly susceptible to ambient light fluctuations and random movements. The test subject needs to remain relatively still in front of the camera, and ambient light fluctuations must be well controlled.

With the advancement of mmWave circuitry and K-band radar technology, measuring micro-movements using K-band radar transceivers appears to be more achievable. K-band radars operate within the frequency range of 24 GHz and 24.25 GHz and are typically used in Doppler radar systems to measure the velocity of moving objects. Aumann and Emanetoglu [5] reported an experimental approach for measuring vibrations in the human chest with a simple K-band transceiver motion sensor. They successfully obtained a cardiogram at an open distance of 6 mm using the experimental setup described in their article. However, this method has two potential limitations: a limited working distance and the presence of fatal null points where signals are completely attenuated within specific ranges. The radar used in this research incorporates a single mixer, and the power is split using a Balun signal splitter. The RX (receiving) signal from the RX antenna directly mixes with the split signal via a diode mixer, with no RF (Radio Frequency) LNAs (Low-noise Amplifiers) used in either the TX (transmitting) or RX (receiving) signal paths.

Vinci *et al.* [6] utilised a six-port radar and a data-acquisition system to achieve non-contact heartbeat and respiration detection over relatively long-range (a few inches), proving more reliable and higher-quality signals. However, due to hardware limitations and a low sampling rate, the useful bandwidth is restricted to less than 100 Hz, making it inadequate for precise cardiovascular diagnosis. Diraco *et al.* proposed a lower-frequency Ultra-Wideband Radar as a measuring sensor for unobtrusive elderly monitoring [7]. Unlike other radar-based approaches, this research uses a pulsed radar with a relatively low frequency (4.3 GHz). The radar operates in pulsed mode with a high pulse repetition rate, and the demodulation algorithm can capture body movement, estimate heart rate and respiration rate, and even detect falls. However, its frequency spectrum can overlap with the 3.1–5.3 GHz range used by various home electronics such as Wi-Fi, smartphones, computers, and other wireless devices. Therefore, that system may encounter signal interference when deployed in a home environment.

Chian *et al.* [8] proposed a method for increasing measuring targets by utilising multiple radar sensors combined with IR cameras where the respiration and heart rate of multiple people can be estimated. For non-invasive cardiopulmonary monitoring, an increased effective range is favourable in certain applications. Certain types of active-controlled radar systems [9–11] have been developed where their working principle is different from classical Doppler radar, they rely on active frequency tracking to eliminate null points and analyse the phase information. However, due to the circuit limitation of the specific approach, the above-mentioned approaches have to work in the lower RF band (2.4 GHz–5.8 GHz) which is more susceptible to interference from communication devices and reflections. Their approach also limits the available bandwidth of the measured signal, some temporal information is lost, and no vibrography and phonography signal is preserved. This limits the application to heart rate measurement only, and such systems cannot obtain phonocardiograms or act as non-contact stethoscopes.

Lauteslager *et al.* [12] proposed a system that uses a contacted radar sensor to estimate the cardiodynamics, the system can measure the artery movements without much pressure applied. Its non-invasive approach and relatively accurate nature make it suitable for diagnosis applications, but its range and capabilities on distant non-contact monitoring are very limited. FMCW radar with beam steering has also been utilised [13] to obtain the precordial movement signs, but the nature of the system has been shown to have a very limited range. FMCW radars are also subjected to time-domain motion aliasing due to their limited special sampling rate, which is controlled by their sweep repetition frequency (SRF). The sweep repetition rate for common FMCW radar is usually under 200 Hz where the cardiac vibration signal and environmental vibrations can easily exceed their Nyquist frequency, causing aliasing artifacts in their measurements which degrades signal quality. Also, due to the nature of FMCW radar distance measuring, it is not easy to do antialiasing on the signals besides increasing SRF. However, the increase in SRF will also cause signal degradation by reducing SNR and spatial resolution.

A few implementations [14,15] focused on utilising advanced radar hardware have been reported and Heterodyne Doppler Radar is often used in combination with frequency-domain extraction approaches. These approaches have shown certain advantages over traditional approaches, but due to their highly complicated and specialised hardware design, as well as the nature that their algorithms lose temporal rhythmic information of the cardiac activities, their application is yet to be a popular choice.

On the opposite side, a few implementations [16–19] focused on low-end, cost-sensitive and performance-limited devices have also been researched. The majority of the implementations attempt to address the limitation when a high-precision DAQ system is unavailable, and the others are mainly focusing on pure analog frontend processing. These implementations had given a useful guide on implementing contactless vital sign measurement in resource-limited conditions, but due to the lack of higher-level processing and analysis techniques, only very limited information can be retrieved for further and deeper analysis of vital signs.

Several pure signal-processing-oriented algorithms have been researched and their principles largely differ from each other. Wang *et al.* [20] experimented with an alternative DACM demodulating algorithm which targets reducing frequency-domain distortion under large movement conditions. Oh *et al.* [21] developed a solution where the heart rate is obtained by eliminating other signals with simple algorithms. Xia *et al.* [22], developed an algorithm which skips the demodulation process and uses a band envelope for cardiac activity detection. Gouveia *et al.* [23] utilised adaptive filtering and frequency approaches to retrieve heart rate information. The latter two implementations are highly partial and specialised algorithms that are only useful for retrieving heart rates. Their implements cannot retrieve phonography and vibrography information.

There are alternative solutions that involve accelerometer-based

detection [24–26] and laser interferometry-based detection [27,28]. However, these methods can hardly be categorised as proper and widely applicable non-contact vital signs monitoring approaches due to their numerous limitations. The accelerometer-based solution requires direct contact with the chest wall to achieve mechanical signal conduction, and the laser interferometry-based solution requires exposed skin, either on the precordia chest wall or directly above the carotid arteries. Choudhary *et al.* [29] outlined a fair review of the accuracy and reliability assessment of laser Doppler vibrometer and traditional Doppler radar on carotid artery measurement. Their applicability in live operative environments and their capacity to offer a generic, non-contact and non-invasive solution is limited.

The majority of the current research focuses on the generic measurement of heart rate and respiration rate [30], but most of the systems have limited usable bandwidth, accuracy or working distance since a large portion of them are using cardiac base-band. They not only cannot obtain phonography and vibrography information but also the cardiac base-band movement is heavily suspected to have different effects. The precordia movement pattern is also not always rich in fundamental frequency where it is very common for the precordia area to have motion that lacks the fundamental frequency, and the cardiac base-band frequency (0.67 Hz–3 Hz) can also be easily overwhelmed by common body motions. These makes those approaches specific and highly vulnerable to motions, to the point they can only applied in completely static conditions or even barely work on certain testing subjects. The loss of temporal information and higher frequency vibrography bands also makes them unable to detect certain arrhythmias or carry out deeper analysis of the vibrography signals.

3. Hardware system

The proposed hardware contains an analog system, a data acquisition system, an embedded system, and an auxiliary system. Fig. 1 illustrates the design diagram (d) and snapshots of the prototype with (b) and without the display (c). The analog system contains RF front-end and signal conditioning components, including filters, compensation,

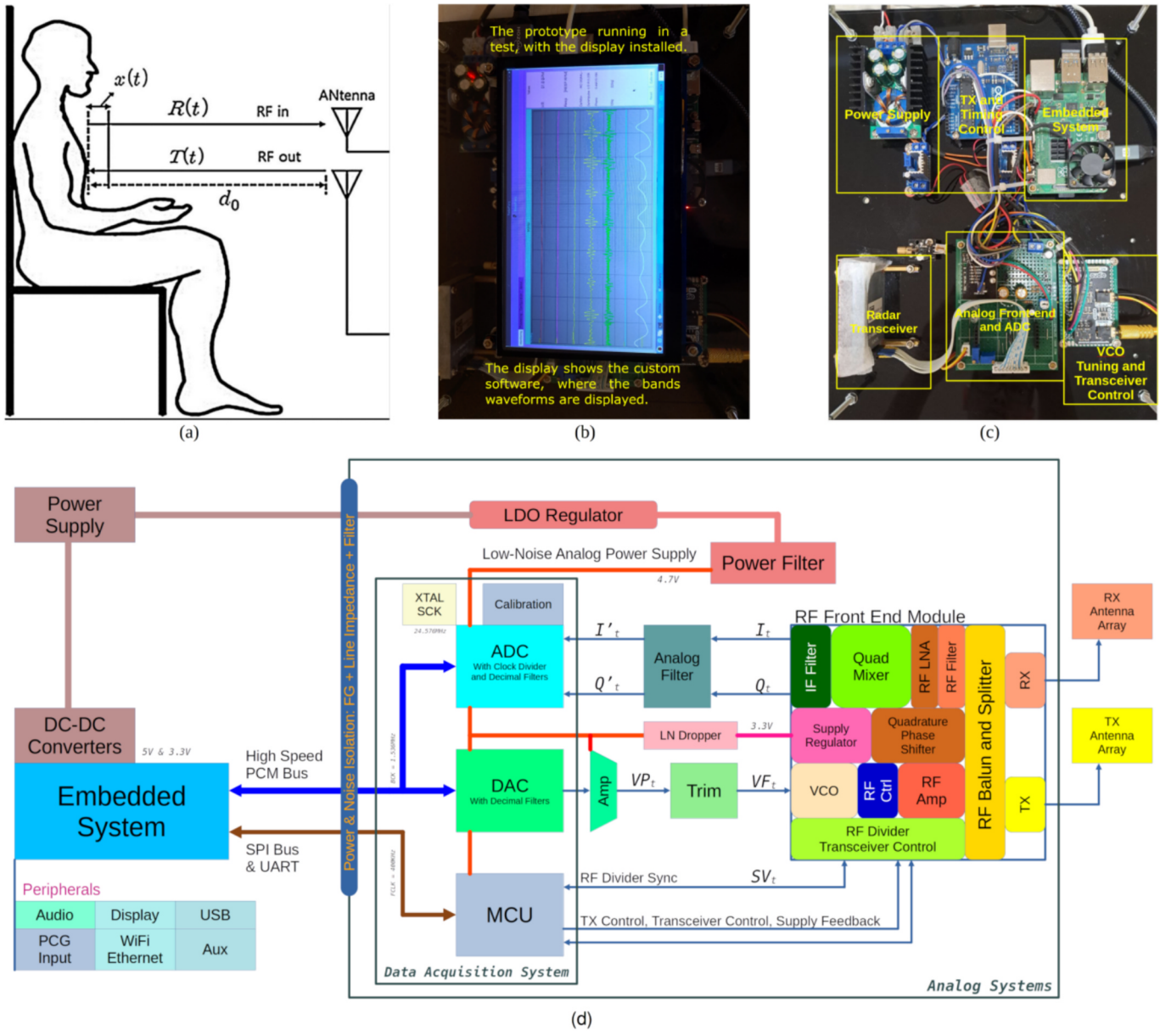

Fig. 1. The proposed hardware system. (a) Deployment mode; (b) A prototype snapshot with the developed software running; (c) A snapshot without the display and the hardware modules labelled; (d) Design system diagram.

and trimming. They are interconnected with the interfaces of the Analog-to-Digital Converter (ADC) and Digital-to-Analog Converter (DAC). The digital interface is then connected to the embedded system using noise-isolated Pulse Code Modulation (PCM) data buses and a floating ground to transmit data and isolate electrical noise from the embedded system. The embedded system is responsible for computational and control tasks, where software, signal processing and RF transceiver control tasks are carried out. The auxiliary systems include the power supply system, display, and expansion systems.

To measure vital signs, the radar transceiver's radio beam must be directed toward the chest and precordia area, as shown in Fig. 1(a), to pick up the cardiological movement signs. An effective working distance of up to 3.2 m (d_0) and a beamwidth spread angle of up to 30 degrees is tolerated, ensuring that the signal reflection is not significantly attenuated. In the prototype device, all systems, including the custom-designed PCBs and the display, are installed on a frame, as shown in Fig. 1(b). The system can be powered with only a DC supply (9 ~ 36 V) or a battery, with no need for external supplies or connections. The details of each system are described below.

3.1. The analog system

The analog system, as the core of the signal collection, is responsible for primary signal conditioning, providing signals for data acquisition, and accepting signals from the transceiver control unit.

3.1.1. RF front-end

The RF front-end consists of a hybrid-mode controllable K-band radar transceiver, which operates based on the Doppler radar principle. Doppler radar is a specific type of radar that utilises the Doppler effect for motion detection. This effect is characterised by the shift in frequency and phase of the reflection wave from a moving object, due to its motion relative to the speed of the wave in the medium.

The Doppler radar transceiver consists of a transmit path and a receive path. In the transmit path, radio waves are generated, modulated, and emitted through the antenna. These waves travel from the antenna to the measuring surface, reflect off the surface, and return to the radar transceiver. A portion of these waves pass through the receiver antenna and are picked up in the receive path. The radar uses the Doppler frequency and phase shift information to demodulate the movement signal into IF (intermediate frequency) signals for further processing. Given the extremely high frequency of the radio waves and the speed of radio waves in the air, the frequency and phase shifts of the reflected waves are insignificant compared to the frequency of the radio waves. As a result, it is impossible for traditional frequency measuring methods to detect minor frequency shifts, especially when the subject's movement is subtle or very slow.

To solve the abovementioned frequency resolution issue, the frequency mixing technique is used to create image frequencies that effectively distinguish the frequency and phase differences between the two signals. Frequency mixing is a technique where image frequencies are generated by mixing the two signals through a non-linear RF mixer. The goal is to shift the frequency information towards lower frequency ranges while preserving other characteristics. Through the frequency conversion achieved by mixing with the original signal, the previously subtle and undetectable Doppler frequency shift can be brought down to the IF band, thereby retaining the frequency shift and phase information. This results in a significantly lower frequency, enabling effective signal detection.

The employed Doppler radar transceiver, illustrated in Fig. 2(a), operates at a frequency of 24 GHz with a usable bandwidth of 250 MHz. It features a tunable voltage-controlled oscillator (VCO), which allows it to function in Continuous-Wave (CW)/Frequency Modulated (FMCW), or Frequency-Shift Keying (FSK) modes. The VCO initially generates low phase-noise RF signals under tuning control and then forwards this signal to an RF amplifier. The amplified signal is then routed to an RF Balun and Splitter, which splits it into two parts. Most of the signal is directed to the RF transmit port, connecting to the TX antenna (shown in Fig. 2(b)). Meanwhile, a minority of the split signal is further divided into two paths for frequency mixing.

One of the divided signal paths passes through a 90-degree phase shifter, converting the local oscillator signal into a complex quadrature signal for complex quadrature signal frequency mixing. The transmitted signal is radiated from the TX antenna and reflected off the measuring surface. The movement and static displacement of the surface induce a frequency and phase shift in the signal when it reflects off the surface and reaches the RX antenna. The reflected signal received by the RX antenna passes through an RF filter to extract the desired frequency band. It is then amplified by an RF LNA to increase the signal amplitude. This amplified signal is then directed to a quadrature mixer to mix with the local quadrature signal, which comprises two non-linear diode frequency mixers that handle in-phase and quadrature signals separately. The mixing process yields a pair of sum-and-difference frequencies, with the sum frequency approximately at 48 GHz and the difference frequency representing the Doppler shift frequency. The obtained Doppler shift frequency is the signal of interest, as it falls within the lower frequency range and can be easily collected and analysed. Therefore, the mixed signal is then passed through another IF filter to eliminate the summed frequency and extract the desired IF signal. The IF output is also in I-Q complex form, where two channels are utilised to construct the

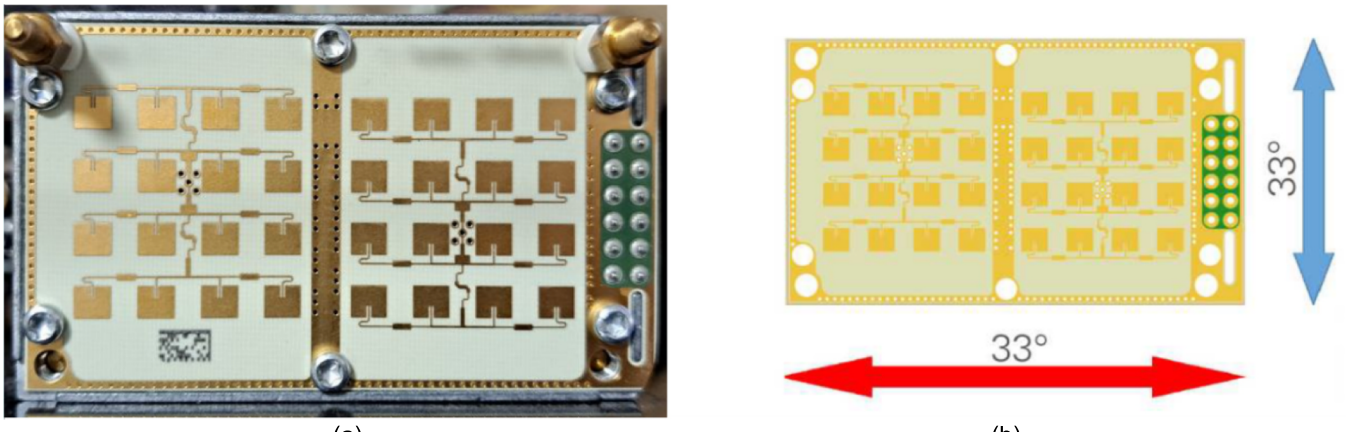

Fig. 2. The radar transceiver (a) The antenna array (RX and TX); (b): The beam angles of the radar.

polar representation of the complex signal. Subsequently, the signals are collected, processed, and demodulated to extract movement and displacement information.

The radar typically operates in the CW mode, where signals are transmitted in a fixed frequency, and the object's movement induces a Doppler shift in the returned frequency. The radar's receiving pathways downshift this Doppler shift frequency and directly output it as a quadrature signal in a complex format. This quadrature signal can then be demodulated using Quadrature Arc-tangent Demodulation (the process of demodulating the phase from quadrature signals), phase unwrapping (the process of unwrapping the limited and wrapped phase sequence of $0 \sim 2\pi$ into a continuous unlimited phase sequence), and phase integration to accurately determine the absolute movement of the measured object. It should be noted that the radar can also operate in the FMCW mode or FSK mode. These modes allow dynamic calibration for the CW mode and the extension of the working distance by sacrificing some of the available bandwidths.

FMCW radar with higher carrier frequencies (for example IWR6843) were considered during the research, but it was not finally used over the 24 GHz implementation, for the following reasons. Typical FMCW radars use sweeps to acquire Doppler frequency information in frames and carry out demodulation for every frame to obtain the ranging distance. This causes a trade-off between sweep repetition frequency (SRF) and SNR. The SRF is the effective sampling rate of the obtained ranging info. Generally, the SRF of such FMCW radars is not expected to be higher than 200 Hz to have a proper SNR. It means that their obtained cardiovascular vibrograph bandwidth can only reach 100 Hz, which is insufficient and lower than this research. Cardiac vibrograph signals have a high bandwidth, especially in the phonography range. Cardiac murmurs can extend up to 1 KHz in bandwidth. Insufficient bandwidth will not only make the system incapable of acquiring PCG but also cause aliases in the lower bands. Our implementation uses a sampling rate of 48 KHz and has an overall usable signal bandwidth of 14KHz with high SNR, allowing it to accurately acquire the whole range of cardiovascular vibrations and sounds in high quality. The VCO is used for ranging proposes and auto compensation. The software automatically issues a VCO sweep at certain times to acquire the distance and the polar centre and uses the acquired information to compensate for the processing and fine-tune the radar.

It should be noted that the 24-GHz K-band radar is selected because the frequency-band is sufficient distant from lower-frequency communication-bands, preventing interference from electronic devices (including Wi-Fi, cellphone signals or Bluetooth). The selected K-band offers a balance between demodulation precision and environment/clothing absorption. Lower-frequency radars have lower demodulation precision, whereas higher-frequency radars suffer from increased environmental and clothing absorption, reducing their working distance and cloth-penetration capabilities. Considering performance, cost, and world-wide legislations for radio frequencies, K-band is selected as the optimal solution.

3.1.2. Signal conditioning

As a specialised device that requires very high processing precision and consists of several different subsystems operating under different conditions, proper noise isolation is vital. The embedded system and the auxiliary systems are the primary sources of power consumption. The embedded processor generates electrical interference, which can lead to power noise affecting the entire embedded system. Therefore, it is important to implement proper power isolation to preserve the signal integrity of the data buses and to isolate noise from the analog systems. In the analog system, multiple low-pass filter circuitries are used to suppress noises and interferences in the outputs of the radar front end. First-order RC low-pass filters with a cut-off frequency at 24 kHz are used to remove interferences above the used bandwidth.

3.2. The data acquisition system

3.2.1. Analog-to-digital converter (ADC)

The radar front-end's RF demodulation converts signals to the IF-frequency band enabling the analysis of frequencies and phases. The complex IF output requires further sampling and digitisation before undergoing digital signal processing (DSP). The core of data acquisition is a high-precision ADC that digitises analog signals with a 24-bit resolution. It then transmits the digitalised signals to the embedded system via the high-speed PCM/I^2S bus. The used ADC is a precise and fast two-channel device with a 105 dB SNR and provides a wide dynamic range. The sample rate is set at 48 kHz to capture a broad range of IF frequencies and amplitudes. It has two channels for capturing the I-channel and Q-channel of the radar front-end's IF output. Unlike some current implementations, the data acquisition works in the CW mode, without interruptions between sample sequence groups. It continuously sends every captured sample to the embedded system. The high sampling rate and superior sampling quality result in a wide effective IF bandwidth with minimal noise and distortion. This high-quality data acquisition provides sufficient bandwidth for acoustical analysis and frequency domain analysis, allowing accurate parsing of different signal bands without the risk of aliasing, distortion, or noise corruption.

The clocks for bus and sampling are generated by the ADC's internal clocking circuitry, driven by a low-drift crystal oscillator. This step creates steady sampling and bus clocks that supply the DAC and the embedded system, both of which are configured in the clock-slave mode.

The ADC's antialiasing and oversampling functions are enabled to further reduce noise that may corrupt the bandwidth in use. The high-pass filter in the ADC is bypassed to preserve the DC component of the IF signal.

This specific type of ADC converter and the configuration is selected for its excellent precision and high bandwidth, as well as extremely low noise-floor and distortion. The sampling clock of the ADC is highly stable, benefiting from a low-drift crystal oscillator and the self-clocking feature of the ADC, preventing distortions caused by clock dithering and jitters. In comparison, I^2C ADCs are more affordable and have simpler interfaces, but they rely on the embedded system for clocking, which inevitably degrades clocking performance. They also have significantly lower sampling rates and SNRs, leading to substantial signal deterioration during the analog–digital conversion stage. In this research, the selected ADC configuration, combined with the noise isolation circuitry, introduces complexity to the system, but the resulting performance is highly beneficial and encouraging.

In real tests, the system achieves an SNR and dynamic range of over 100 dB, resulting in a ranging accuracy of 30 nm. In the acoustic pickup experiments, the surface vibration caused by sound waves is clearly audible in the demodulated signals with the application of proper filtering and gain, and it exhibits negligible distortion and noise. This forms a solid and reliable foundation for the implementation of advanced algorithms and medical-grade signal analysis.

3.2.2. Digital-to-analog converter (DAC)

To enable the radar to operate in different modes, it is necessary to generate a proper analog VCO tuning signal and feed it to the radar VCO control input. While hardware oscillators may be used for this purpose, they lack several important functionalities when compared to generating the signal through DSP. DSP can produce arbitrary waveforms at various frequencies, intervals, and amplitudes, providing highly flexible control for the radar system. Generating the control signal using DSP requires its conversion into analog waveforms to control the radar VCO. This task is handled by the DAC system.

The DAC module used in this study is a high-performance two-channel device with a 24-bit resolution and a remarkable 106 dB SNR. It is connected to the embedded system via the high-speed PCM/I^2S bus in a synchronised and passive configuration. The entire bus operates at the same data sampling rate to prevent resampling and mitigate any

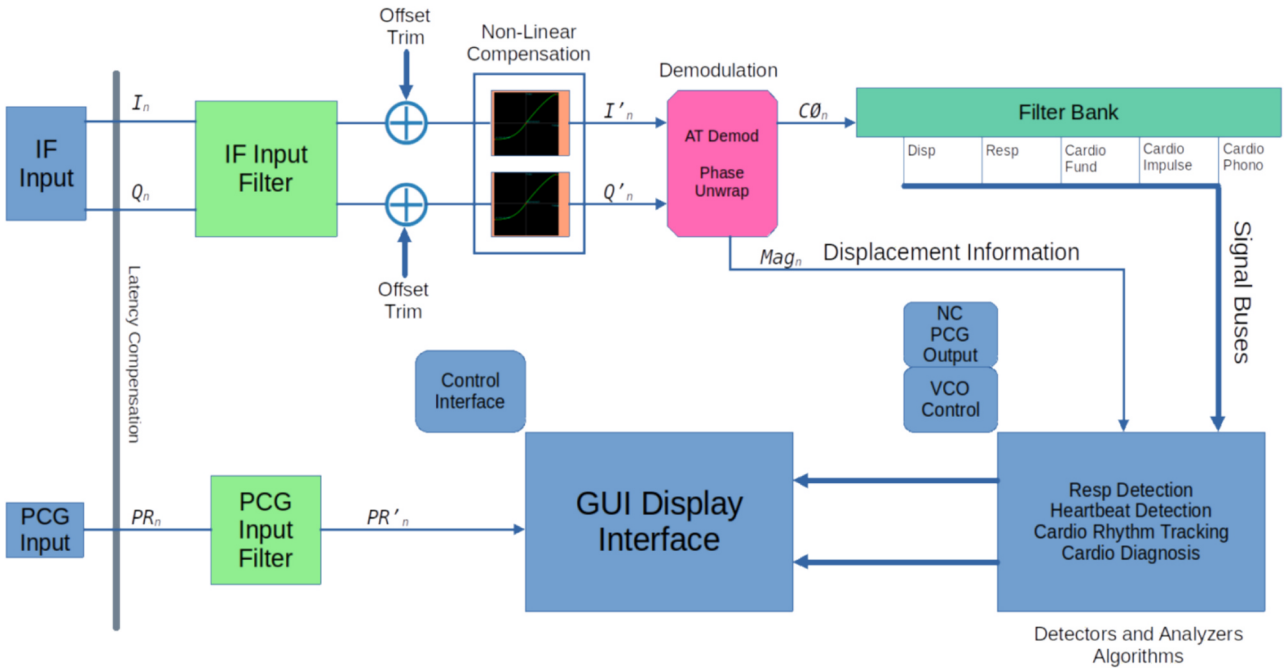

Fig. 3. The software and algorithm flow diagram.

potential dithering effects.

3.3. The embedded system

The embedded system serves as the core hardware of the entire system, responsible for all signal processing and analysis tasks. The prototype employs an ARM-based embedded system featuring 4 core Cortex-A72 cores and 8 GB of RAM. A critical component of this system is the high-speed PCM/I^2S bus, which provides a stable and precise sampling clock to the embedded system. Operating in the clock slave mode, the embedded system eliminates the need to generate its own sampling clock from the internal clock generator, thus mitigating the clock dithering effect. It has its own FIFO buffers and DMAs (Direct Memory Access) for PCM/I^2S bus I/O. This configuration allows the system and software to provide data samples in small chunks instead of one sample at a time. This block-based signal processing approach reduces the need for hard real-time compliance that requires processing samples one by one at the sampling rate as any dropped samples or delays in a real-time system can lead to information loss, artifacts or processing errors. The hardware-buffer-assisted block-based processing addresses the need for a hard real-time system and preserves the data streaming nature for timely analysis.

3.4. The auxiliary system

The prototype hardware is a highly self-contained system, and it makes effective use of the expandability of the embedded system. It includes a dedicated touchscreen display (Fig. 1(b)) for interactive and flexible user interactions. Additionally, it features several peripheral ports and wireless systems, which are supported and utilised to extend its functionality. The onboard audio of the embedded system is also utilised for non-contact stethoscope applications. Medical professionals can utilise the system for diagnosis, and if they prefer to use stethoscope auscultations as part of their diagnostic process, the system can also function as a non-contact stethoscope. In this mode, the phono-band signal obtained from the demodulated radar signal is further processed and then outputted via the onboard audio to earphones or headphones worn by the medical professional. This approach not only provides supreme audio quality and high resistance to environmental noises but also eliminates the need for physical contact with a stethoscope, thus reducing the risk of cross-infections associated with stethoscope contact.

4. Algorithm and software

The software deploys the developed algorithms for control, signal processing and analysis. As depicted in Fig. 3, the software framework designed for this system takes raw sampled data from the hardware, performs signal processing, demodulation, filtering, detection, and analysis, and generates signals for radar VCO tuning control. The software offers a set of well-developed functionalities and provides a user-friendly graphical user interface (GUI) for user interaction. Users can easily modify and save multiple configurations within the software, eliminating the need for hardware calibration adjustments. The algorithms include three major parts: Demodulation, Filtering, and Heartbeat Detection Analysis, which are detailed below.

4.1. Demodulation

The demodulation process transforms raw IF quadrature signals from the radar into the desired accumulated phase and amplitude information. The radar's front end features a complex quadrature mixer, resulting in two output channels that form a complex quadrature signal, phased 90° apart. These two channels trace a polar circle on the complex plane, where the rate of polar angle progression represents the object's speed, and the polar magnitude represents the reflected signal intensity. To demodulate the signal, the channels first need to be mapped to the polar centre of the complex plane by a series of compensation processes. For this application and specific hardware, static compensation is performed to account for changes in the radar antenna, typically caused by self-cluttering variations. Dynamic calibration is also available during runtime and automatically employs the trace of the IF signal's polar plots to determine the polar centre, which can be achieved by conducting a cycle of FMCW sweeps. After the signals are mapped via compensations, the polar angle can be converted to phase, and the phase can be unwrapped, and integrated to provide precise information about the movement of the measured object.

The phase unwrapping process involves considering the previous

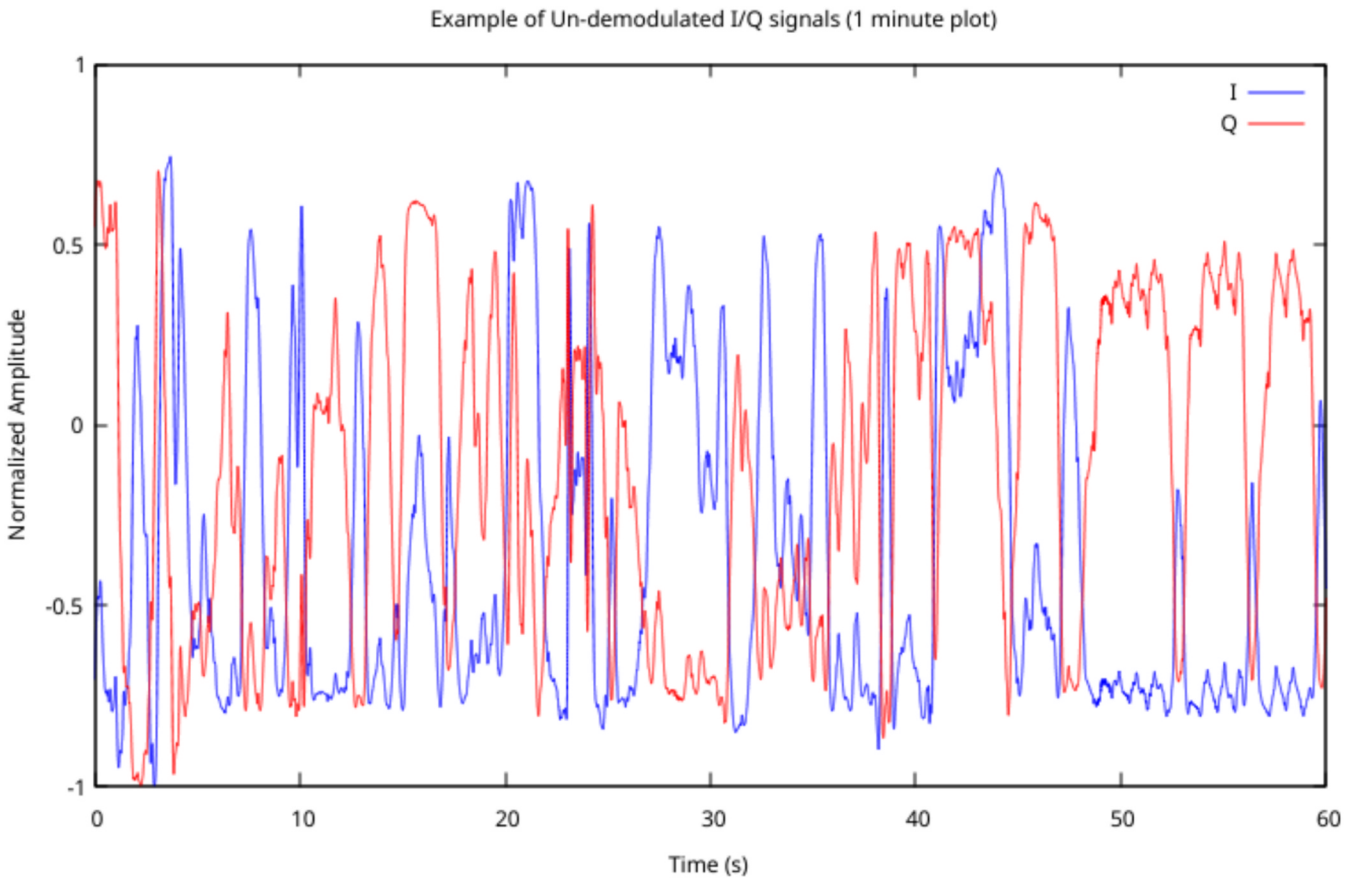

Fig. 4. The example of I/Q signal acquired (1-minute duration plot).

phase history along with the current phase value and utilising phase progression trends. The samples consist of discrete pairs of real and imaginary components of the complex IF signal at the time of sampling. These samples do not directly indicate the phase progression and direction within the sample itself. Therefore, referencing the previous sample and ensuring signal conditions comply is important. In this process, the polar angle and the location of the current complex sample are computed. These values are then compared with the previous polar angle and the location of the last complex sample. This comparison results in two progression orbits, each morphing the previous sample and the current sample in different directions, with one being shorter than the other. Thanks to the high sampling rate relative to the effective bandwidth of IF signals, a strong contrast is achieved, making it easier to select the shortest progression path. This, in turn, facilitates the determination of its polar angle progression. The phase can be then unwrapped and integrated to derive the movement on an infinite abstract ranging scale, which is determined by the wavelength. The high sampling rate also ensures that aliasing in demodulation will not occur. Fig. 4 shows an example of raw I/Q signals acquired for a 1-minute duration.

Theoretically, this technique allows for an infinite working distance, but practical limitations still apply. Radio waves tend to scatter and are weakly absorbed by the air and the measured surface. As a result, reflected signals weaken when the measured surface is too far from the radar. The amplitudes of the obtained IF signals also weaken due to the nature of the frequency-mixing down-conversion process. When the signal becomes extremely weak, it can affect the demodulation process. Our prototype system has undergone testing and can effectively measure objects within a working distance of up to 3.2 m under ideal conditions, where cluttering and reflections are controlled and limited. As detailed in Section 3, the system is immune to interferences from common electronic devices and has good tolerance for environmental absorptions. However, clutter and reflections could still have some impacts on the result. The effective working distance may be reduced in environment with highly reflective surfaces to the radio waves, such as metallic wall.

4.2. Filtering

The filtering process involves passing the obtained signals through filter banks, which separate the signals into different bands. Filtering is carried out to the demodulated and unwrapped signal that represents precordia and chest wall movement. The precordia area exhibits a highly symbolic movement and vibration pattern, containing all the necessary information for detecting heartbeats and respiration. Traditionally, this information is retrieved using a stethoscope or accelerometer. In this study, it is captured by radar with associated demodulation, providing higher signal quality and lower distortion.

The obtained raw precordia signal, after demodulation, is a superposition of different signals, including body movement displacement, respiration-related chest movements, heartbeat-induced chest movements, impulses from heart contraction, and heartbeat sounds (vibrations). As a result, five corresponding bands can be parsed to obtain signals that reflect various aspects of the cardiopulmonary system.

In the filter design process, a series of discrete biquad filter units are used to construct each complex filter within a band filter, a method known as parametric filter design. Biquad filters are favoured for their computational accuracy, ease of achieving stability, and flexible design patterns.

A biquad filter is given by the transfer function:

$$H(z) = \frac{b_0 + b_1 z^{-1} + b_2 z^{-2}}{a_0 + a_1 z^{-1} + a_2 z^{-2}} \tag{1}$$

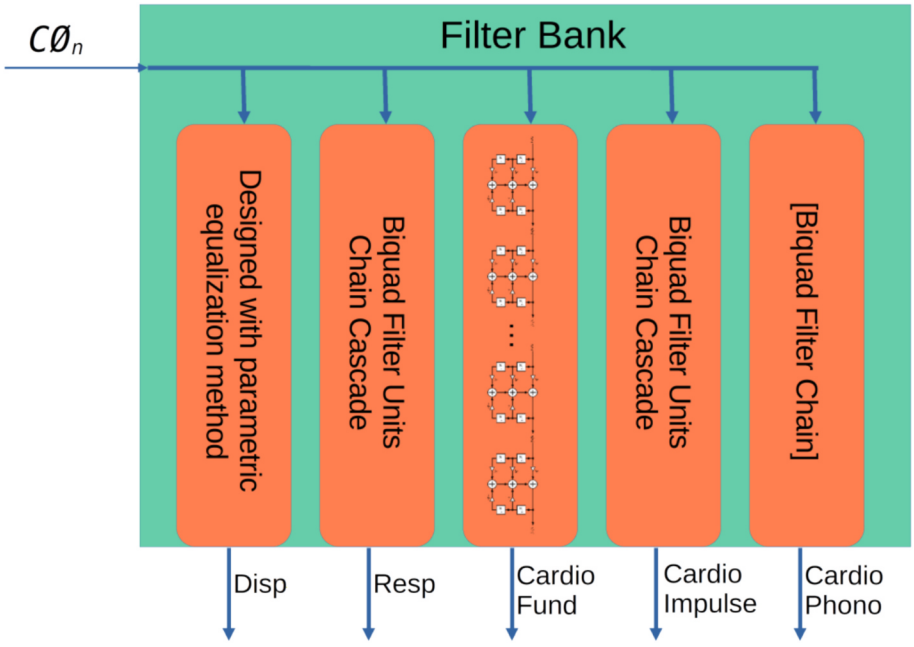

Fig. 5. The structure of the filter bank and the cascading filters. The interconnection structure of multiple biquad filter units is shown in the middle channel (Cardio Fund).

which can be written in the discrete differential equation for computation:

$$y[n] = \frac{1}{a_0}(b_0x[n] + b_1x[n-1] + b_2x[n-2] - a_1y[n-1] - a_2y[n-2]) \tag{2}$$

A template exists for each basic filter type, where the parameters are derived from transfer functions of second-order continuous-signal filters. Parameters are employed to control the frequency, gain and Q-factor/bandwidth/shelf-coefficient of the filter unit. They can be arbitrarily placed to create the desired filter shape and response. The filter coefficients are generated dynamically to adapt to various sampling rates.

The Filter unit design starts with a set of constants

$$A = 10^{(\frac{dBgain}{40})} \tag{3}$$

$$\omega_0 = \frac{2\pi f_0}{Fs} \tag{4}$$

$$\begin{aligned}\alpha &= \frac{\sin(\omega_0)}{2Q} \quad (\text{for case Q}: \text{ Q} - \text{factor}) \\ &= sin(\omega_0)\sinh(\frac{\ln(2)}{2}\frac{\text{BW}\omega_0}{\sin(\omega_0)}) \quad (\text{for case BW}: \text{ Bandwidth Octaves}) \\ &= \frac{\sin(\omega_0)}{2}\sqrt{(\text{A} + \frac{1}{A})(\frac{1}{S} - 1) + 2} \quad (\text{for case S}: \text{ Shelf} - \text{Coefficient})\end{aligned} \tag{5}$$

where f_0 is the filter centre frequency, F_S is the sampling rate, and Q, BW and S are the filter slope parameters and types respectively.

The filter coefficients a_0-a_2 and b_0-b_2 can be then calculated with the following formulas according to the filter types and the calculated constants in Eqs. (3)–(5).

Low-Pass Filter:

$$a_0 = 1+\alpha \quad b_0 = \frac{1-\cos(\omega_0)}{2}$$

$$a_1 = -2cos(\omega_0) \quad b_1 = 1-cos(\omega_0)$$

Table 1
Filter Parameters for the five bands.

Band	Type	Frequency	Gain	Mode	Slope Rolloff
Displacement	Low-pass	0.1 Hz	0 dB	Q-Mode	1.0 Q
Respiration	High-pass	0.1 Hz	0 dB	Q-Mode	1.0 Q
	Low-pass	1.0 Hz	0 dB	BW-Mode	1.0 Oct
Cardio Fund	High-pass	0.85 Hz	0 dB	Q-Mode	1.3 Q
	High-pass	1.0 Hz	0 dB	BW-Mode	0.707 Oct
	Low-pass	5.5 Hz	0 dB	Q-Mode	1.0 Q
Cardio Impulse	High-pass	6.5 Hz	0 dB	Q-Mode	1.0 Q
	High-pass	10 Hz	0 dB	BW-Mode	0.707 Oct
	Peaking-EQ	15.7 Hz	15 dB	Q-Mode	0.85 Q
	Low-pass	35 Hz	0 dB	Q-Mode	1.0 Q
Cardio Phono	High-pass	18.5 Hz	0 dB	Q-Mode	1.0 Q
	High-pass	20.0 Hz	0 dB	Q-Mode	1.0 Q
	Low-pass	100 Hz	0 dB	BW-Mode	1.414 Oct

$$a_2 = 1-\alpha \quad b_2 = \frac{1-\cos(\omega_0)}{2} \tag{6}$$

High-Pass Filter:

$$a_0 = 1+\alpha \quad b_0 = \frac{1+\cos(\omega_0)}{2}$$

$$a_1 = -2cos(\omega_0) \quad b_1 = -(1+cos(\omega_0))$$

$$a_2 = 1-\alpha \quad b_2 = \frac{1+\cos(\omega_0)}{2} \tag{7}$$

Peaking EQ filter:

$$a_0 = 1+\alpha/A \quad b_0 = 1+\alpha A$$

$$a_1 = -2cos(\omega_0) \quad b_1 = -2cos(\omega_0)$$

$$a_2 = 1-\alpha/A \quad b_2 = 1-\alpha A \tag{8}$$

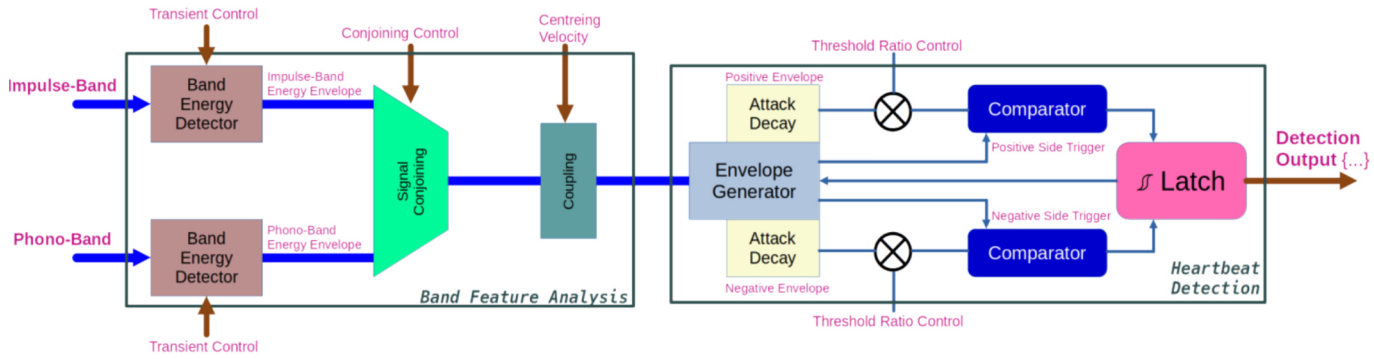

Fig. 6. The heartbeat detection algorithm simplified flow diagram.

After generating the coefficients, the filter unit can process the given signal with Eq. (2). The processing involves applying the new input value, evaluating Eq. (2), and iterating the input histories (x) and output histories (y). Multiple designed biquad filters are then cascaded in series to create a complex filter, where the design criteria are defined by a unified set of parameters describing the desired response. This method enables the easy design and implementation of highly complex filters. Higher-order filters can be achieved by replicating the same filter unit as needed. The frequencies and parameters of the five band filters, shown in Fig. 5, are tailored to match the characteristics of each band to optimise performance. The outputs are then directed to various analysis units for detection and analysis. The parameters of each band in the filter bank, summarised in Table 1, are selected according to their nature and are dynamically adjustable.

In the experiments, similar methods such as wavelet decomposition, EMD and other non-linear techniques are explored when choosing the used algorithm for real-time heartbeat detection. As a result, a configurable parametric filter bank is discovered to be the best performing algorithm in terms of robustness, real-time performance and computational costs. The windowed processing techniques (including EMD and Wavelet methods) utilises long windows which cause largely increased detection latency; some of the methods are also relatively computational expensive under real-time processing on real-time embedded systems. The configurable filter bank is tuned accordingly to the characteristic frequencies of the human cardiovascular system, which are relatively consistent across different subjects. Combined with the adaptive latching detection with band-energy envelope conjoining, the filter bank method provides a real-time friendly and reliable method for the application.

4.3. Heartbeat detection and analysis

The process of heartbeat detection and analysis, as depicted in Fig. 6, involves real-time detection of the heartbeat by analysing specific bands and subsequently providing a primary diagnosis of cardiovascular conditions. The key band of interest is the impulse band, as it exhibits a signal with high contrast and is not susceptible to interference from body movements or speech activities. The cardio fund band might be affected by body movements. The signals of the impulse band and phono band are processed to extract the band energy envelopes. They are conjoined by correlation or multiplication to suppress noise and emphasise the heart contraction peaks. It is then coupled to remove offset and centred. By performing such a band feature analysis, the complicated oscillation patterns of the impulse band and phono-band are converted to robust monotonic waveforms representing cardiac contractions. The envelope generator generates a positive envelope and a negative envelope with a slow and adjustable decay factor, which is used as an auto-adapting and reference threshold for the band feature waveform. The comparator compares the band feature waveform and the generated threshold envelopes to obtain the upstroke and the downstroke. The latch provides a strong hysteresis which is able to suppress artifacts and noises. The upstroke detection is outputted as the indication of heart contraction and the per-beat heart rate can be obtained by calculating the heartbeat intervals. The detailed pseudocode is presented in Algorithm 1.

Algorithm 1 – The pseudocode for the heartbeat detection algorithm

```
1   procedure E_vp(input) returns: generated negative envelope
2     decay_envelope_p is memory variable
3     attack_ratio is constant [0 ~ 1]
4     if input > decay_envelope_p
5       decay_envelope_p ← input × attack_ratio + decay_envelope×(1-
    attack_ratio);
6     else
7       decay_envelope_p ← exponential_decay(decay_envelope_p, time_constant);
8     return decay_envelope_p;
9     end if
10  end procedure
11
12  procedure E_vn(input) returns: generated negative envelope
13    decay_envelope_n is memory variable
14    attack_ratio is constant [0 ~ 1]
15    if input < decay_envelope_n
16      decay_envelope_n ← input × attack_ratio + decay_envelope×(1-
    attack_ratio);
17    else
19      decay_envelope_n ← exponential_decay(decay_envelope_n, time_constant);
20    return decay_envelope_n;
21    end if
22
23  end procedure
24  function E_n is Hilbert envelope or windowed RMS.
25  function C_j is correlation or multiplication.
26
27  procedure LATCH_RISE is a latched detection with hysteresis and 100 ms
    deadtime.
28  procedure RUN_DETECT
29    for each sample
30      impulse_band_filter_bank_output ==>
    impulse_band_rolling_window_buffer;
31      phono_band_filter_bank_output ==> phono_band_rolling_window_buffer;
32      impulse_band_energy ← E_n(impulse_band_rolling_window_buffer,
    impulse_transient);
33      phono_band_energy ← E_n(phono_band_rolling_window_buffer,
    impulse_transient);
34      conjoined_energy ← C_j(impulse_band_energy, phono_band_energy);
35      SET_COUPLING_HIGHPASS_FILTER_PARAM(order, centreing_velocity);
36      combined_feature_value ← COUPLING_HIGHPASS(conjoined_energy);
37      T_p ← E_vp(combined_feature_value) × positive_threshold_ratio;
38      T_n ← E_vn(combined_feature_value) × negative_threshold_ratio;
39      positive_triggered ← COND(combined_feature_value > T_p);
40      negative_triggered ← COND(combined_feature_value < T_n);
41      if LATCH_RISE(positive_triggered, negative_triggered) then
42        beat_interval = samples_between_beat ÷ sample_rate;
43      per_beat_heart_rate = 60 ÷ beat_interval;
44      OUTPUT(per_beat_heart_rate);
45      end if
46      samples_between_beat ← samples_between_beat + 1;
47    end for
48  end procedure
```

Table 2
The results of the instrumental tests.

Test	Parameters	Performance
1	Effective DAQ Bandwidth (±3dB)	0 ~ 22 kHz
1	SNR* (Electrical and DAQ System)	101 dB
2	Effective Radar Pickup Bandwidth (±3dB)	0 ~ 14 kHz
2	SNR (small signal pick-up)	99.7 dB (BW† = 3 kHz)
2	Large signal non-linear distortion	0.02 % (T_{ramp}§ = 3 s, $X_{p\text{-}p}$¶ = 30 mm)

* SNR: Signal-to-Noise Ratio;
† BW: Bandwidth (Applied Signals);
§ T_{ramp}: Ramp-Time;
¶ $X_{p\text{-}p}$: Peak-to-Peak excursion (of the test actuator).

5. Results

5.1. Instrumental tests

The instrument test aims to assess the hardware and software systems using artificially generated testing signals. These testing signals were generated via programs at a sampling rate of 48 kHz. The analogue signal generator used for this purpose is a high-precision and high-speed USB DAC without any added signal processing, and it includes a built-in signal amplifier to ensure proper signal amplitudes.

The first test evaluates the digital acquisition system, with the radar module disconnected. In this setup, the generated signals were directly fed into the DAQ channels and then converted by the ADC. This setup tests the electrical performance of the DAQ system. The second test evaluates the radar system's performance for small and large signals, respectively, including a comprehensive assessment of the entire radar system's signal pathway and demodulating algorithms. The SNR was calculated by comparing signal amplitude and non-signal components (noise and distortion). The "small signal test" evaluates the frequency response and impulse response of the radar system. In these two tests, sine waves were used to measure the SNR, and impulses and white noise were employed to evaluate the effective bandwidth. The "large signal test" assesses the response of high-amplitude signals and the linearity of the system. Repeating ramps were used in this test to evaluate the linearity of the pickup and demodulation. These tests were performed by electrical–mechanical transducers including a piezoelectric disc and a specific speaker driver, respectively. The piezoelectric disc, known for its excellent frequency bandwidth and flat response, was used to test the bandwidth and response of the radar and signal pathways. The transducers are used in their linear frequency and amplitude ranges.

Table 2 provides a summary of the performance results in the instrumental tests, including the bandwidth, SNR, and pickup and

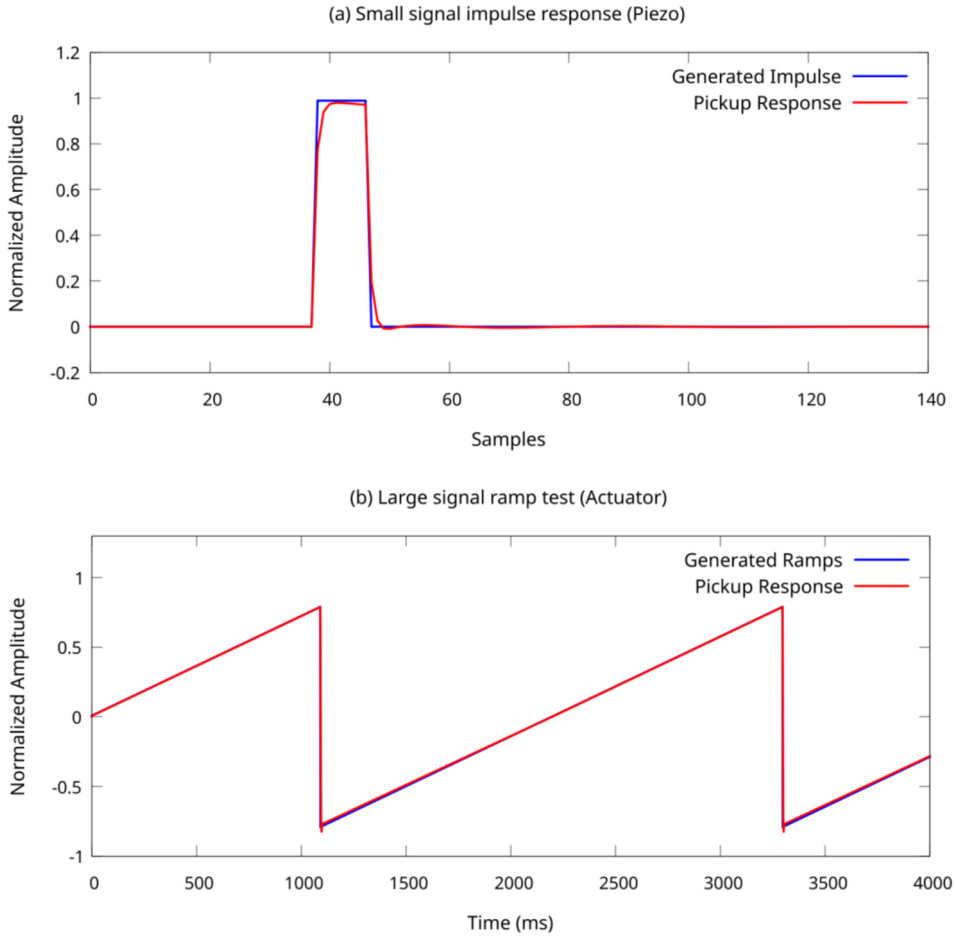

Fig. 7. The radar pickup and demodulation small signal short impulse response (a) and the large signal ramp response test (b).

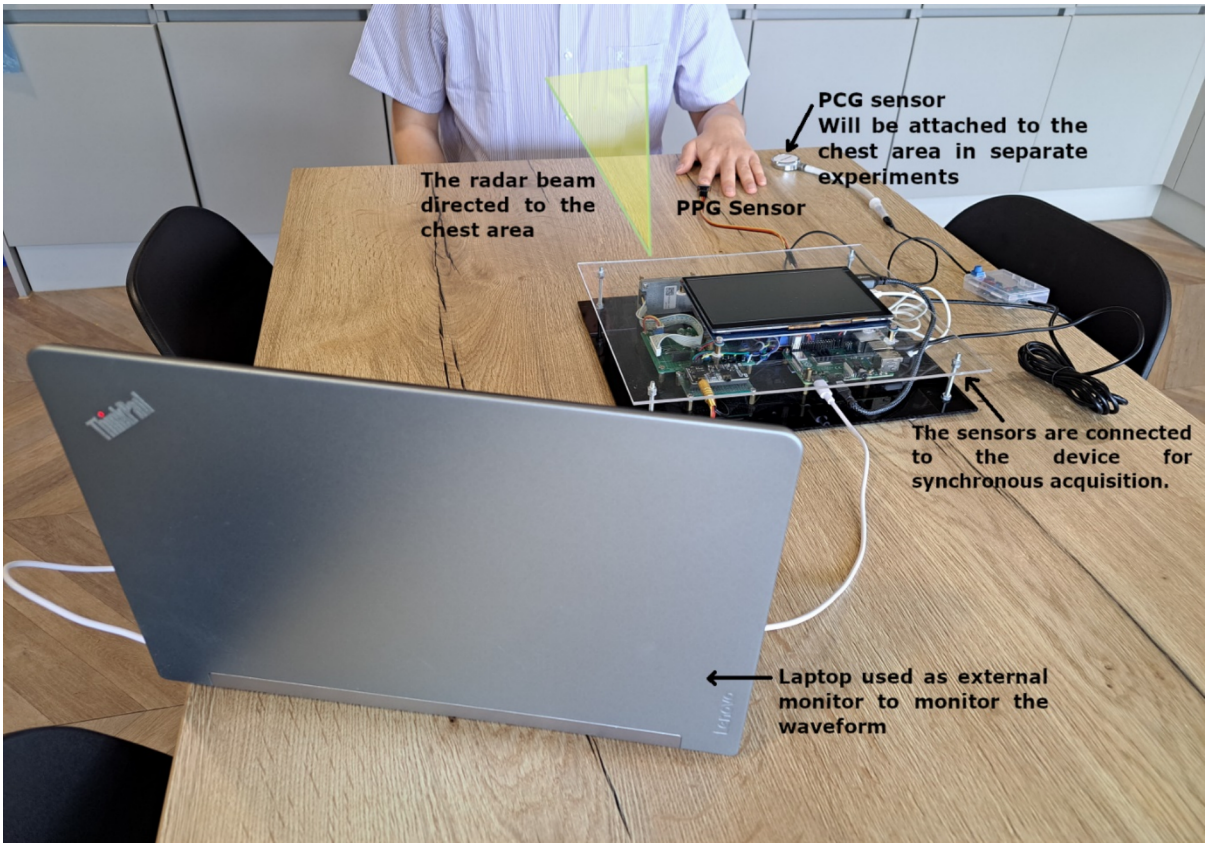

Fig. 8. Demonstration of the experiment setup that was carried out in a relatively large room with controlled environment. The prototype device is directing towards the test subject's chest area. The ground-truth reference sensors (PPG and PCG) are connected to the device for synchronous acquisition and comparison.

Table 3
The quantitative results of the experimental tests.

No.	Age/Gender	Condition	RRMSE	Absolute Error (Beats per minute)[§]	P value[†]	Apnea Indication[¶]
1	23/M	Sitting with movements	0.98 %	0.72 ± 0.41	<0.001	No
2	23/M	Sleeping and waking up	0.52 %	0.31 ± 0.26	<0.001	No
3	31/M	Standing and talking	0.84 %	0.69 ± 0.57	<0.001	No
4	24/F	Sitting completely static	0.88 %	0.51 ± 0.44	<0.001	No
5	23/M	During and after sport	0.91 %	0.94 ± 0.67	<0.001	No
6	26/F	During yoga-alike exercise	0.97 %	0.67 ± 0.48	<0.001	Yes

[†] Two tailed, paired T-test applied for each sequence, consisting 600 sample points.
[¶] Apnea indication from the program monitor.
[§] The mean of the absolute error between the measurement and the ground-truth reference ± standard deviation of the absolute error.

demodulation linearity from the first and second tests. In the first test, the analog system and data acquisition system achieved a bandwidth of 22 kHz and a high SNR of 101 dB. The second test demonstrates that the radar pickup and demodulation systems achieve a high SNR of 99.7 dB for small signals and nonlinear distortion of only 0.02 % for large signals. More detailed evidence, demonstrating the fine performance of the proposed system, is presented in Fig. 7. This figure compares the generated signals (impulse and ramp) and their corresponding pick-up response. It is important to note that the bandwidth of the small signal pickup SNR test is limited to 3 kHz due to the distortion of the piezoelectric transducer around its resonant frequency.

5.2. Experimental tests

In this test, the ground truth of measurement is provided using a PCG and PPG (medical grade MAX30102) sensor, both of which were integrated with the prototype. PCG and PPG sensors are selected for comparisons as their functionalities and working natures are highly similar to this research. The experiment setup is shown in Fig. 8. The PCG sensor, functioning as a sensitive electronic stethoscope, can pick up heart sounds. It serves as a means for qualitative comparison with the phono band of the proposed system. However, it should be noted that PCG signals cannot be precisely numerically compared with the phono band due to the non-linear phase response and non-uniform frequency response of the PCG sensor. Therefore, an envelope comparison and spectrum comparison were carried out to evaluate the correctness of signals. The validation of the heartbeat analysis was performed by comparing the measured heart rates obtained from the proposed non-contact method and those obtained using the PPG method. It tests the overall system performance with a focus on evaluating the software algorithms. The results were validated by comparing the obtained heart rate sequences and calculating the Relative Root Mean Squared Error (RRMSE).

The experiments are categorised into static conditions and dynamic conditions. Static conditions involve static seating, lying down, and standing, to emulate common daily life situations or static measuring

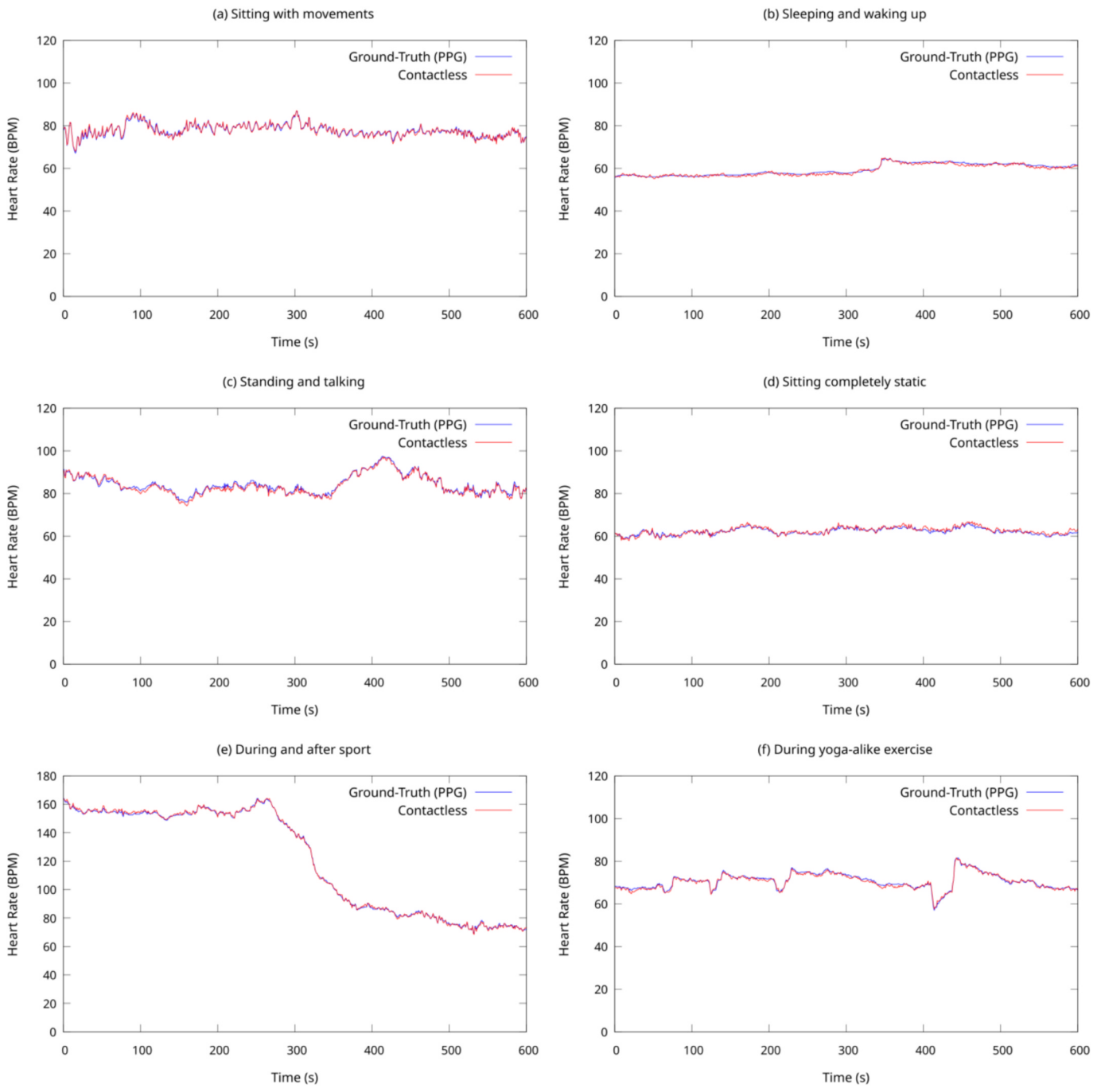

Fig. 9. Results of the experimental test under static and dynamic conditions. (a) sitting with movements, (b) sleeping and waking up, (c) standing and talking, (d) sitting completely static, (e) during and after sport, (f) during yoga-alike exercise.

procedures during medical diagnoses. The specific body movement patterns include stretching, twisting and moving, which is meant to be the opposite of complete stationary to prove the system's ability to measure consistently under reasonable movement. Dynamic conditions involve moving subjects and measuring them after physical activities, to validate the system's performance under live scenarios besides the daily circumstances. For each test, data was recorded for a duration of 10 min and the cardiac rhythm and heart rate were measured in real-time, with all the heart rate data points being read out at one sample per second to generate the heart rate plot. All the experiments were carried out at a working distance of 1 m between the prototype device and the testing subject.

Table 3 displays the qualitative test results on different test subjects under different conditions. RRMSE, its 95 % confidence interval, and P values for all tests are calculated. For each test, an RRMSE value of under 1 % was obtained and the P value was calculated to be under 0.001.

Fig. 9(a)–(f) displays a comparison of heart-rate measurements obtained from the proposed system (red curves) and those from the PPG sensor (blue curves) for the subject under various physical conditions. The majority of the contactless traces closely match the PPG reference traces. Only minor differences can be observed in certain tests, possibly caused by minor PPG interferences due to limb movements. These results demonstrate that this contactless system has a similar performance to the contact-based PPG sensor. To further quantify the performance, Table 4 presents the RRMSE values for all six tests. It is evident that the maximum error is less than 1 % when compared to the ground truth.

Table 4
Comparison of different systems for measurement of heart rate and respiration.

Approach	Range	Accuracy	Temporal information & vibrography	Motion immunity
CW	Medium	Low	NO	Low
Cardiac Base Band	(<1 m)	(up to 20 % error) [31,32]		
FMCW	Medium-Long	Medium	NO	Medium
Cardiac Base Band	(<1.5 m typ.)	(up to 10 % error) [33]		
Frequency-Tracking	Long	Medium	NO	High
Or Pulse Radar	(2 ~ 3 m typ.)	(up to 10 % error)		
Time domain	Short	Medium-High	Limited (10 s heartrate calculation resolution)	Low
Quadrature Radars analysis without demodulation	(<0.3 m)	(up to 5 % error)		
The proposed system	Long	High	Per-beat Information; PCG; Virtual Stethoscope	High
	(up to 3.2 m)	(up to 1 % error)		

There is no significant difference between various static and dynamic conditions, while as expected, the sleep condition achieved the best performance. Additionally, the system successfully detects apneas caused by deliberate breath holds in yoga-like exercises due to reduced activity in the respiratory band.

Fig. 10 depicts a quantitative comparison between the reference PCG recording and the Phono-Band of the proposed system. The two waveform traces are recorded and displayed in synchronisation. The radar beam was directed at the same precordia area where the PCG sensor was attached. The waveform traces exhibit a high degree of similarity in their comparable features. The minor observable differences in the traces are a result of the strict band roll-offs of the contactless phono-band compared to the natural response of the reference PCG. Fig. 11 is a spectrum plot of the above signals for better visualisation of high similarity in the frequency domain.

Fig. 12 plots the detailed traces and the exported apnea detection event markers, indicated by the "A" above the time axis. A total of 5 apneas are detected in the experiment session where the first 4 apneas are the instructed breath holds in the exercise and the last apnea is likely to be an irregular breath during talking. The instructed breath holds also cause a significant change in the heart rate which is highly visible in the graph.

To further investigate the impact of the working distance on SNR, we conducted an additional experiment where the distance was varied from 20 cm to 5 m with a step of 20 cm. Fig. 13 plots the RRMSE values between the heart rate measurements from the proposed system and PPG at different working distances. It can be observed that the system achieved an RRMSE lower than 5 % for working distances shorter than 3.2 m. After 3.2 m, the accuracy of measurements sharply deteriorates.

5.3. Discussion

Compared to existing related works, the proposed system delivers highly accurate heart rate measurements with high temporal resolutions across a range of conditions and distances. As shown in Table 3, our system achieves an error of less than 1 % in experimental tests, whereas most comparable systems report errors in the range of 5 % to 20 %, as detailed in Table 4. The evaluation methodology aligns with those used in related studies, where errors are calculated by comparing system outputs to ground-truth references such as PPG, wristbands, or ECG signals. Additionally, the proposed system supports a relatively long working distance of up to 3.2 m, while most existing systems operate within 2 m. It is also worth noting that although some systems targeting heart rate measurement over a wide range of distances can achieve comparable resolution, they often rely on complex decomposition algorithms that require extended measurement times and do not provide temporal or vibrography information.

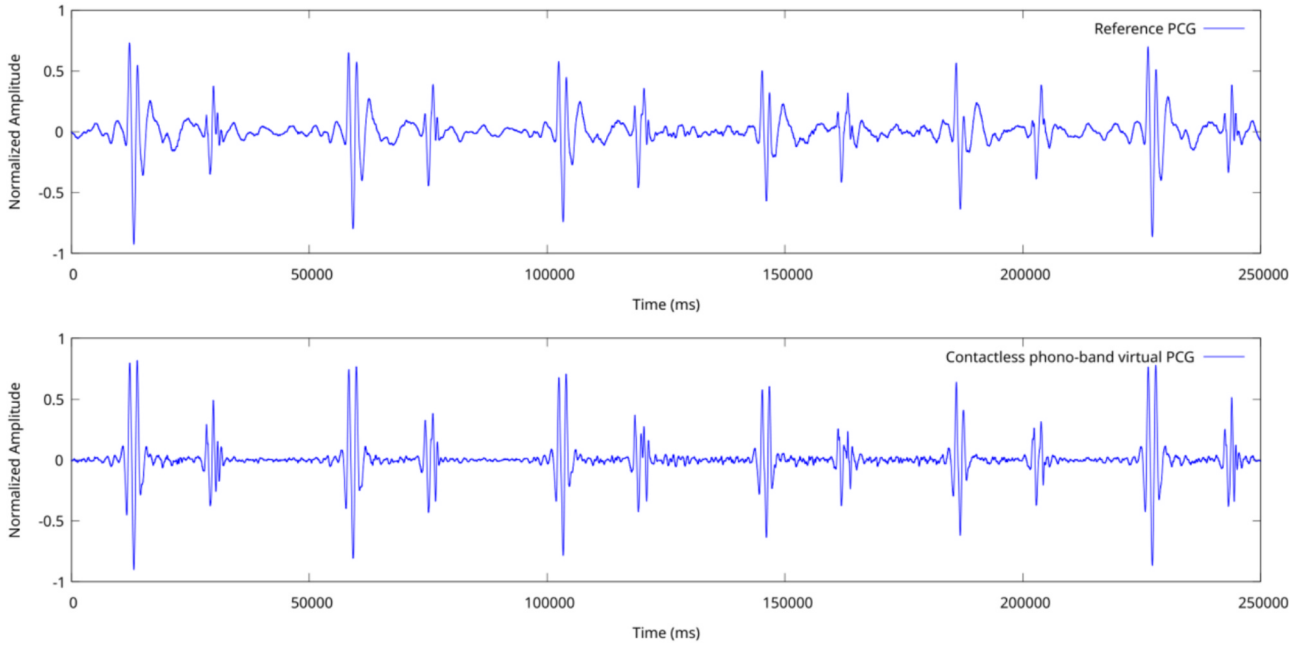

Fig. 10. The qualitative comparison between reference PCG (top) and the contactless phono-band (bottom).

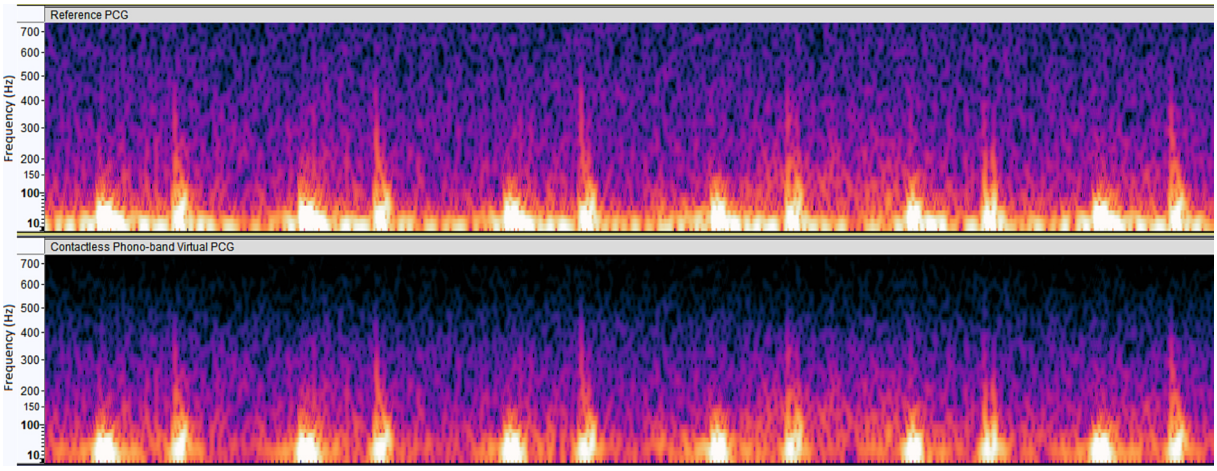

Fig. 11. The spectrogram comparison between reference PCG (top) and the contactless phono-band (bottom).

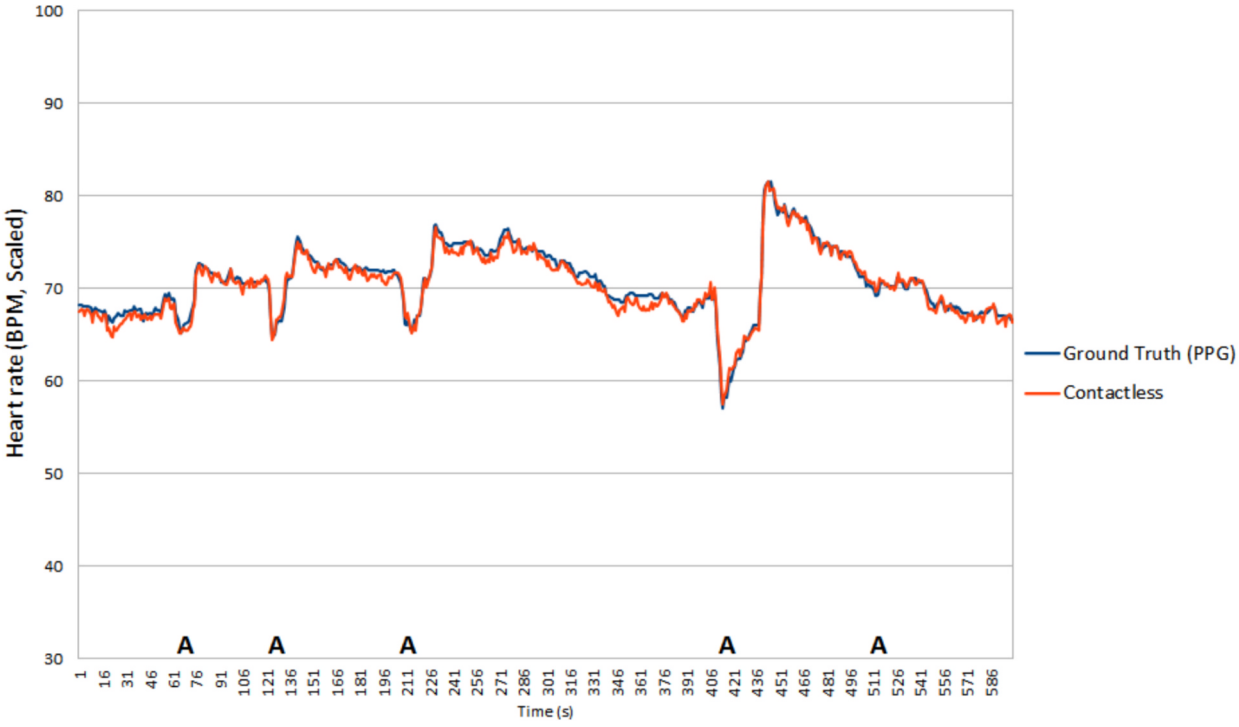

Fig. 12. Apnea indications markers added in contrast with the test with breath holds.

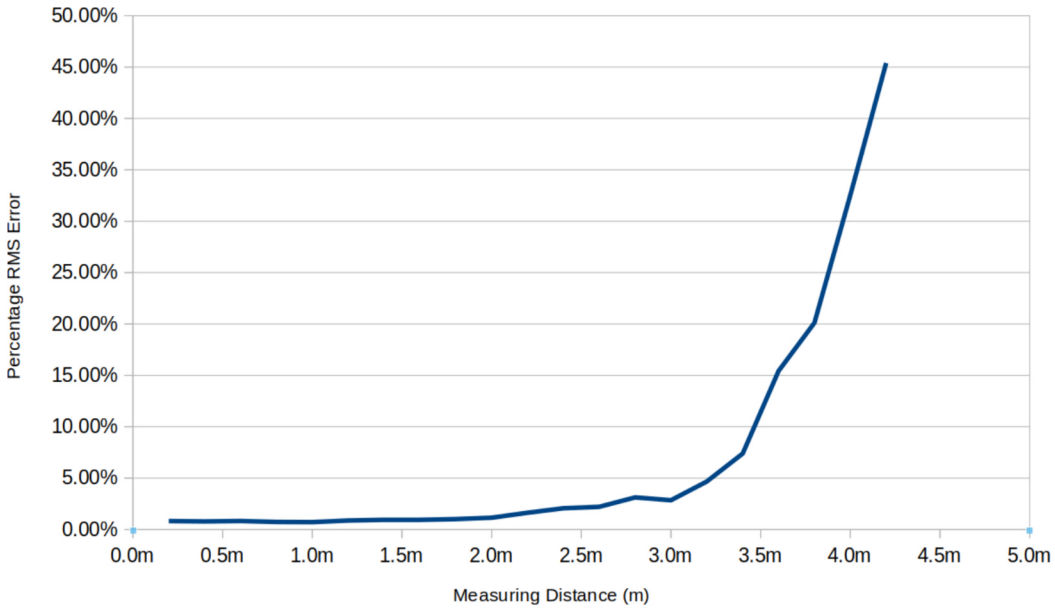

Fig. 13. The RRMSE percentages of heart-beat measurements against different working distances.

6. Conclusion

Contactless vital signs monitoring offers a wide range of potential applications including critical personnel monitoring, home and healthcare monitoring, self-assisted public health devices, and rescue operations. In critical personnel monitoring, this non-invasive and contact-free method can monitor safety–critical personnel, such as vehicle drivers and machine operators, without interfering with their ongoing operations. Existing studies mainly focus on heartrate estimation using contactless sensors, but their application and practical values are relatively limited. Most of them are limited in working distance, temporal resolution, and detection accuracy, and they usually lack real-time monitoring capabilities. In this research, we have designed, developed, and validated a novel system for the precise and contactless measurement of human vital signs. The novelty of this work includes:

(1) The solution integrates an advanced Doppler radar front-end, a robust data acquisition system, and specialised signal processing algorithms, leading to superior performance across in a range of tests. The results have demonstrated that the system can achieve real-time accurate per-beat heart rate and rhythm measurements with a relative root mean squared error of less than 5 % for a working distance of up to 3.2 m (less than 1 % RRMSE for a working distance of 1 m), with subjects both static and in motion.
(2) The proposed approach and algorithms are highly robust against motion artifacts. Existing studies typically use the cardiac base band (0.67 Hz–3 Hz) for heartbeat detection, which could be susceptible to interference from common body motions. Considering the characteristic frequencies of the human cardiovascular system, we propose using the impulse band (10–35 Hz, with a peaking frequency at 15.7 Hz adopted in this study) to mitigate interference caused by body movements or speech activities.
(3) The parametric filter-bank allows for real-time separation of individual frequency band, while the heartbeat detection algorithm is robust and reliable for real-time monitoring. Although the filter-bank approach is not new to ARM architectures, a parametric filter-bank is rarely used on radar-based heartrate monitoring systems. Most radar-based heartrate systems use long-windowed spectrum or decomposition approach that cannot operate in real time and often compromise temporal resolution.

Real-time monitoring can timely detect or even predict potential major life-threatening conditions, providing early warnings to individuals or organisations to prevent potential disasters. Within healthcare systems, the proposed system can reduce physical contact while enhancing diagnosis efficiency, by functioning as a stethoscope or a cardiovascular monitor without the need for direct skin contact, reducing the risk of infection and lightening the workload of healthcare professionals. In rescue operations, this technology is especially vital in situations where physical contact with individuals is highly difficult or impossible, such as in confined spaces or when dealing with severe injuries. The system is highly self-contained and can be extended relatively easily to wired or wireless internet for remote operations. It can also be deployed in various operational environment benefiting from a long working distance and tolerance to interferences from common communication radio waves and electronics.

While promising results have been achieved in various tests, the system has certain limitations and room for improvement. The first consideration is the miniaturisation of the hardware by reducing the size of the PCBs and optimising the use of spaces within the casing. This would enhance the portability of the hardware and expand its applications, particularly for systems with geometrically intricate spaces, such as vehicles. Another concern relates to device vibration cancellation. The current tests were carried out under relatively static conditions, and if the device operates in an environment with vibrations, the quality of the obtained signals may be compromised. To address this issue, a potential solution is to integrate an accelerometer and gyroscope module into the device. This module can measure its own vibrations and then compensate for them in the software. Moreover, this contactless measurement can also be further integrated and conjoined with other contactless biological signs measuring devices, such as induction-based non-contact ECG. The integrated system will be capable of measuring various aspects of vital biological signs, thus providing greater versatility for a wide range of applications. In the future, additional tests will also be carried out on larger and broader groups of subjects, including patients with cardiovascular disease and respiratory diseases, to provide solid evidence of the system's abilities across a broader demographic and wider range of health conditions. Further work will also focus on encapsulation, system integration, and provision of a standard interface to facilitate cloud integration, thereby enhancing the system's applicability and impact.

CRediT authorship contribution statement

Qi Yong: Writing – original draft, Writing – review & editing, Visualization, Validation, Methodology, Investigation, Formal analysis, Data curation. **Yifan Zhao:** Writing – review & editing, Validation, Supervision, Resources, Project administration, Funding acquisition, Conceptualization.

Declaration of competing interest

The authors declare that they have no known competing financial interests or personal relationships that could have appeared to influence the work reported in this paper.

Data availability

Data will be made available on request.

References

[1] B. Zhang, H. Li, L. Xu, L. Qi, Y. Yao, S.E. Greenwald, Noncontact heart rate measurement using a webcam, based on joint blind source separation and a skin reflection model: for a wide range of imaging conditions, J. Sens. 2021 (2021) e9995871, https://doi.org/10.1155/2021/9995871.

[2] M. Lewandowska, J. Ruminski, T. Kocejko, J. Nowak, Measuring pulse rate with a webcam – a non-contact method for evaluating cardiac activity. Federated Conference on Computer Science and Information Systems – FedCSIS, 18–21, Szczecin, Poland, 2011.

[3] I. Bush, Measuring Heart Rate from Video, Stanford Computer Science, 2016.

[4] M. Kayani, M.M. Riaz, A. Ghafoor, N. Iltaf, Pulse rate extraction based on local-area motion magnification, Measurement 152 (2020) 107290, https://doi.org/10.1016/j.measurement.2019.107290.

[5] H.M. Aumann, N.W. Emanetoglu, A radiating near-field 24 GHz radar stethoscope, PubMed (2018) 5121–5124, https://doi.org/10.1109/embc.2018.8513478.

[6] G. Vinci, S. Lindner, F. Barbon, M. Hofmann, G. Fischer, D. Kissinger, A. Koelpin, 24 GHz six-port medical radar for contactless respiration detection and heartbeat monitoring, IEEE Xplore (2012) 75–78. https://ieeexplore.ieee.org/abstract/document/6450726.

[7] G. Diraco, A. Leone, P. Siciliano, A radar-based smart sensor for unobtrusive elderly monitoring in ambient assisted living applications, Biosensors 7 (4) (2017) 55, https://doi.org/10.3390/bios7040055.

[8] D.-M. Chian, C.-K. Wen, C.-J. Wang, M.-H. Hsu, F.-K. Wang, Vital signs identification system with Doppler radars and thermal camera, IEEE Trans. Biomed. Circuits Syst. 16 (1) (2022) 153–167, https://doi.org/10.1109/tbcas.2022.3147827.

[9] K. Naishadham, J.E. Piou, L. Ren, A.E. Fathy, Estimation of cardiopulmonary parameters from ultra wideband radar measurements using the state space method, IEEE Trans. Biomed. Circuits Syst. 10 (6) (2016) 1037–1046, https://doi.org/10.1109/tbcas.2015.2510652.

[10] M. Mercuri, Y.-H. Liu, I. Lorato, T. Torfs, A. Bourdoux, C. Van Hoof, Frequency-tracking CW Doppler radar solving small-angle approximation and null point issues in non-contact vital signs monitoring, IEEE Trans. Biomed. Circuits Syst. 11 (3) (2017) 671–680, https://doi.org/10.1109/tbcas.2016.2647560.

[11] M. Mercuri, Y.-H. Liu, I. Lorato, T. Torfs, F. Wieringa, A. Bourdoux, C. Van Hoof, A direct phase-tracking doppler radar using wavelet independent component analysis for non-contact respiratory and heart rate monitoring, IEEE Trans. Biomed. Circuits Syst. 12 (3) (2018) 632–643, https://doi.org/10.1109/tbcas.2018.2813013.

[12] T. Lauteslager, M. Tommer, T.S. Lande, T.G. Constandinou, Coherent UWB radar-on-chip for in-body measurement of cardiovascular dynamics, IEEE Trans. Biomed. Circuits Syst. 13 (5) (2019) 814–824, https://doi.org/10.1109/tbcas.2019.2922775.

[13] S. Fan, Z. Deng, Q. Du, P. Pan, S. Yuan, X. Huang, Radiofrequency Doppler echocardiography, Measurement 220 (2023) 113305, https://doi.org/10.1016/j.measurement.2023.113305.

[14] Gu. Changzhan, C. Li, J. Lin, J. Long, J. Huangfu, L. Ran, Instrument-based noncontact Doppler radar vital sign detection system using heterodyne digital quadrature demodulation architecture, IEEE Trans. Instrum. Meas. 59 (6) (2010) 1580–1588, https://doi.org/10.1109/tim.2009.2028208.

[15] S. Kazemi, A. Ghorbani, H. Amindavar, D.R. Morgan, Vital-sign extraction using bootstrap-based generalized Warblet transform in heart and respiration monitoring radar system, IEEE Trans. Instrum. Meas. 65 (2) (2016) 255–263, https://doi.org/10.1109/tim.2015.2482230.

[16] H. Zhao, H. Hong, L. Sun, Y. Li, C. Li, X. Zhu, Noncontact physiological dynamics detection using low-power digital-IF Doppler radar, IEEE Trans. Instrum. Meas. 66 (7) (2017) 1780–1788, https://doi.org/10.1109/tim.2017.2669699.

[17] D. Tang, J. Wang, W.-W. Hu, Z. Peng, Y. Chiang, C. Li, A DC-coupled high dynamic range biomedical radar sensor with fast-settling analog DC offset cancelation, IEEE Trans. Instrum. Meas. 68 (5) (2019) 1441–1450, https://doi.org/10.1109/tim.2018.2888917.

[18] M. Chen, O. Boric-Lubecke, V.M. Lubecke, 0.5-um CMOS implementation of analog heart-rate extraction with a robust peak detector, IEEE Trans. Instrum. Meas. 57 (4) (2008) 690–698, https://doi.org/10.1109/tim.2007.911629.

[19] Y. Yang, C. Gu, Y. Cao, R.M. Gale, C. Li, Doppler radar motion sensor with CMOS digital DC-tuning VGA and inverter-based sigma-delta modulator, IEEE Trans. Instrum. Meas. 63 (11) (2014), https://doi.org/10.1109/tim.2014.2313032.

[20] J. Wang, X. Wang, L. Chen, J. Huangfu, C. Li, L. Ran, Noncontact distance and amplitude-independent vibration measurement based on an extended DACM algorithm, IEEE Trans. Instrum. Meas. 63 (1) (2014) 145–153, https://doi.org/10.1109/tim.2013.2277530.

[21] S.H. Oh, S. Lee, S.M. Kim, J.H. Jeong, Development of a heart rate detection algorithm using a non-contact doppler radar via signal elimination, Biomed. Signal Process. Control 64 (2021) 102314, https://doi.org/10.1016/j.bspc.2020.102314.

[22] W. Xia, Y. Li, S. Dong, Radar-based high-accuracy cardiac activity sensing, IEEE Trans. Instrum. Meas. 70 (2021) 1–13, https://doi.org/10.1109/TIM.2021.3050827.

[23] C. Gouveia, D. Albuquerque, P. Pinho, J. Vieira, Bio-radar cardiac signal model used for HRV assessment and evaluation using adaptive filtering, IEEE Trans. Instrum. Meas. 71 (2022) 1–10, https://doi.org/10.1109/tim.2022.3190035.

[24] F. Jacobs, J. Scheerhoorn, E. Mestrom, J. Stam, R. Arthur Bouwman, S. W. Nienhuijs, Reliability of heart rate and respiration rate measurements with a wireless accelerometer in postbariatric recovery, PLoS One 16 (4) (2021) e0247903–e, https://doi.org/10.1371/journal.pone.0247903.

[25] C. Romano, E. Schena, D. Formica, C. Massaroni, Comparison between chest-worn accelerometer and gyroscope performance for heart rate and respiratory rate monitoring, Biosensors 12 (10) (2022) 834, https://doi.org/10.3390/bios12100834.

[26] D.H. Phan, S. Bonnet, R. Guillemaud, E. Castelli, N.Y.P. Thi, Estimation of respiratory waveform and heart rate using an accelerometer. Proceedings of the 2008 30th Annual International Conference of the IEEE Engineering in Medicine and Biology Society, 2008.

[27] X. Zhan, Y. Sun, F. Xiao, Y. Meng, J. Zhang, Research on the measurement of heart rate based on LD laser and multimode fiber, IEEE Xplore (2020), https://doi.org/10.1109/OGC50007.2020.9260428.

[28] L. Antognoli, S. Moccia, L. Migliorelli, S. Casaccia, L. Scalise, E. Frontoni, Heartbeat detection by laser Doppler vibrometry and machine learning, MDPI Biosens. J. (2020), https://doi.org/10.3390/s20185362.

[29] T. Choudhary, M. Das, M.K. Bhuyan, L.N. Sharma, Vibrocarotidography: a novel measurement technique to quantify pulsations at common carotid arteries, IEEE Trans. Instrum. Meas. 70 (2021) 1–8, https://doi.org/10.1109/tim.2021.3115203.

[30] J. Kranjec, S. Beguš, G. Geršak, J. Drnovšek, Non-contact heart rate and heart rate variability measurements: a review, Biomed. Signal Process. Control 13 (2014) 102–112, https://doi.org/10.1016/j.bspc.2014.03.004.

[31] X. Zhang, X. Yang, Y. Ding, Y. Wang, J. Zhou, L. Zhang, Contactless simultaneous breathing and heart rate detections in physical activity using IR-UWB radars, Sensors 21 (16) (2021) 5503, https://doi.org/10.3390/s21165503.

[32] S.K. Pramanik, S.M.M. Islam, Through the wall human heart beat detection using single channel CW radar, Front. Physiol. 15 (2024) 1344221, https://doi.org/10.3389/fphys.2024.1344221.

[33] L.J. Dirksmeyer, A. Marnach, D. Schmiech, A.R. Diewald, Developing of algorithms monitoring heartbeat and respiration rate of a seated person with an FMCW radar, Adv. Radio Sci. 19 (2021) 195–206, https://doi.org/10.5194/ars-19-195-2021.

https://dspace.org/

A contactless human vital sign monitoring system using a Doppler radar

Yong, Qi; Zhao, Yifan

2025-12-01
Elsevier
https://doi.org/10.1016/j.bspc.2025.108223
Yong Q, Zhao Y. (2025) A contactless human vital sign monitoring system using a Doppler radar. Biomedical Signal Processing and Control, Volume 110, December 2025, Article number 108223

Downloaded from a DSpace repository. https://dspace.org/